*materials*

MDPI

*Article*

# The Effect of A-Cation and X-Anion Substitutions on the Electronic and Structural Properties of $A_2ZrX_6$ 'Defect' Perovskite Materials: A Theoretical Density Functional Theory Study

**Christina Kolokytha [1,2], Nektarios N. Lathiotakis [1,*], Andreas Kaltzoglou [1], Ioannis D. Petsalakis [1] and Demeter Tzeli [1,2,*]**

[1] Theoretical and Physical Chemistry Institute, National Hellenic Research Foundation, 48 Vassileos Constantinou Ave., GR-11635 Athens, Greece; kolokythac28@chem.uoa.gr (C.K.); akaltzoglou@eie.gr (A.K.); idpet@eie.gr (I.D.P.)

[2] Laboratory of Physical Chemistry, Department of Chemistry, National and Kapodistrian University of Athens, GR-15784 Zografou, Greece

* Correspondence: lathiot@eie.gr (N.N.L.); tzeli@chem.uoa.gr (D.T.)

**Abstract:** In the present work, nine 'defect' perovskites with the chemical formula $A_2ZrX_6$ have been studied, where the A-site cations are a methylammonium cation, formamidinium cation, and trimethyl-sulfonium cation and the X-site anions are halogen, X = Cl, Br, and I. We employ periodic DFT calculations using GGA-PBE, MBJ, HSEsol, and HSE06 functionals. All studied compounds exhibit a wide-bandgap energy that ranges from 5.22 eV to 2.11 eV, while for some cases, geometry optimization led to significant structural modification. It was found that the increase in the halogen size resulted in a decrease in the bandgap energy. The choice of the organic A-site cation affects the bandgap as well, which is minimal for the methylammonium cation. Such semiconductors with organic cations may be utilized in optoelectronic devices, given the substantial benefit of solution processability and thin film formation compared to purely inorganic analogs, such as $Cs_2ZrX_6$.

**Keywords:** hybrid organic-inorganic materials; optoelectronic properties; hybrid DFT calculations



Academic Editors: Carlos Lodeiro and Fabrice Goubard

Received: 31 December 2024
Revised: 24 January 2025
Accepted: 2 February 2025
Published: 6 February 2025

**Citation:** Kolokytha, C.; Lathiotakis, N.N.; Kaltzoglou, A.; Petsalakis, I.D.; Tzeli, D. The Effect of A-Cation and X-Anion Substitutions on the Electronic and Structural Properties of $A_2ZrX_6$ 'Defect' Perovskite Materials: A Theoretical Density Functional Theory Study. *Materials* **2025**, *18*, 726. https://doi.org/10.3390/ma18030726



## 1. Introduction

In recent decades, there has been substantial interest in perovskite materials, encompassing both experimental and computational studies [1–4]. Numerous recent studies have focused on developing new materials and examining the crystal structure and optoelectronic and thermoelectric properties of perovskites. These materials have garnered attention due to their promising features, including low-cost fabrication, adjustable bandgap energies, high absorption coefficients, impressive defect tolerance, and their lightweight, flexible nature, making them ideal for applications where weight and form factor are crucial. The most common applications of perovskites are in laser crystals [5], light-emitting diodes (LEDs) [5,6], solar cells [7], transistors [8], memories [9], superconductors [10], photocatalysts [11], photo electrolysis [4], photodetectors (PDs), and other optoelectronic devices [4,12].

Metal-halide perovskites with the chemical formula $ABX_3$, where the A-site contains an inorganic cation such as cesium or an organic one such as the methylammonium cation (MA) or the formamidinium cation (FA), the B-site typically contains a divalent metal like

$Pb^{2+}$, $Sn^{2+}$, or $Ge^{2+}$, while the X site represents a halogen anion (Cl, Br, or I), have been considered very promising in solar energy conversion for third-generation solar cells [8]. In these systems, the A-site cations appear in twelve-fold coordination with the anions, while the B-site cations are in six-fold coordination. The power conversion efficiency of perovskite solar cells has seen a notable rise, reaching up to 20% in some cases [13–15]. Apart from solar cells, metal-halide perovskites are also well-suited for use in light-emitting devices: In 2015, Stranks and Snaith explored three-dimensional organic–inorganic metal-halide perovskites ($MAPbI_{3-x}Cl_x$ and $MAPbI_{3-x}Br_x$), which exhibited internal quantum efficiencies ranging from 0.4% to 3.5% and emitted light in the near-infrared and green spectra [7]. Serious challenges to be addressed for metal-halide perovskites are the metal toxicity (e.g., in the case of Pb) and their stability. Aiming to address the stability of such compounds, the use of trimethylsulfonium ($(CH_3)_3S$) cation (TMS) as a substitute for the hygroscopic cations has been proposed [16], leading to a series of $(CH_3)_3SPbX_3$ compounds that are very stable at ambient conditions but with a bandgap that exceeds 3 eV, limiting their performance as absorbers in solar cells.

Another subfamily of perovskites (known also as 'defect' perovskites of the $K_2PtCl_6$ archetype) with the stoichiometry $A_2BX_6$, where B is a tetravalent metal cation (Zr, Sn, or Te), has also received significant attention. These compounds hold significant potential for a broad range of applications [12,17]. Cucco et al. theoretically investigated the electronic properties of $Cs_2BX_6$, where B = Sn, Te, Zr, and found tunable electronic and optical properties for hole and electron transport [12]. Abfalterer et al. theoretically synthesized and studied $Cs_2ZrX_6$ (X = Cl, Br) perovskite derivatives, observing a very good agreement between theory and experiment [17]. The obtained bandgaps for these systems were found to be indirect, with values of 5.06 and 3.91 eV for Cl and Br, respectively. Dai et al. reported observing the novel metal halide $((CH_3)_4N)_2ZrCl_6$ exhibiting excitation-dependent luminescence across the full visible region [18]. Lin et al. explored the optical regulation of $A_2ZrX_6$ perovskites, focusing on the host–guest interaction effect by introducing several guestdoping ions, providing insights into the compositional engineering of such compounds [19]. Recently, Tagiara et al. synthesized yet another member of this subfamily, $(TMS)_2ZrCl_6$, with broad photoluminescence [20]. Zr-based compounds are yet largely unexplored, in contrast to their Sn (IV) analogs. Most research so far has been performed on $Cs_2ZrCl_6$, some has been performed on $Cs_2ZrBr_6$, and very limited has been focused on $Cs_2ZrI_6$; mainly, $ZrI_4$ and its adducts are not stable in the air and need to be handled strictly under inert conditions. In contrast to the $Cs_2ZrX_6$ that are prepared by melting the inorganic precursors at ca. 500 °C [21,22], the synthesis of their organic counterparts $A_2ZrX_6$ (A = TMS, MA, and FA) can only be performed at lower temperatures up to ca. 150 °C, either in solid state or in organic solutions. However, the recent synthesis of $TMS_2ZrCl_6$ [20] opens the way for further experimental exploitation in this class of compounds.

Perovskite materials are categorized according to their bandgap energy into three groups: (a) narrow-bandgap perovskites ($E_{gap}$ < 1.4 eV), (b) intermediate bandgap perovskites ($E_{gap}$ around 1.4–1.6 eV), and (c) wide-bandgap (WBG) perovskites ($E_{gap}$ > 1.7 eV). The bandgap is crucial for the determination of the material applications. Thus, materials with a bandgap of about 4–5 eV are considered wide-bandgap semiconductors, with applications as UV detectors and high temperature sensors, in the design of deep UV light-emitting diodes, and in high-power electronics, optoelectronics, etc. Materials with a bandgap around 3.5 eV are also considered appropriate as photocatalysts, UV detectors, UV lasers, thermal sensors, in optoelectronic devices, and in deep UV light-emitting diodes. Materials with a bandgap around 2.8–1.5 eV present many applications in solar cells, as photocatalysts, in LEDs, in optoelectronics, in photovoltaics for blue and UV, and as thin-film transistors. Specifically, a bandgap around 2.5 eV allows it to absorb visible

light in the blue, a bandgap of 1.9 eV allows it to absorb visible light, particularly toward the red, while a bandgap of 1.5 eV is particularly well suited for a range of energy and optoelectronic applications due to its ability to efficiently absorb and emit visible and near-infrared light [23,24].

In the present computational study, we investigate metal-halide perovskites with the chemical formula $A_2ZrX_6$, where the A-site cations are the methylammonium cation ($MA^+$; $CH_3NH_3^+$), the formamidinium cation ($FA^+$; $CH(NH_2)_2^+$), and the trimethylsulfonium cation ($TMS^+$; $(CH_3)_3S^+$) and the X are anions of halogens. Our aim is to reveal the effect of substituting the halogen anion (X-site anion), i.e., $Cl^-$, $Br^-$, and $I^-$, as well as the A-site cation on the calculated bandgap.

## 2. Computational Details

The present theoretical study is based on DFT calculations using the Viena Ab initio Simulation Package (VASP) code, which implements the projected augmented wave (PAW) pseudopotential method [25–27]. Every structure was energetically optimized at the generalized gradient approximation (GGA) level, employing the Perdew–Burke–Ernzerhof (PBE) exchange-correlation functional [28]. Based on the agreement of the structural properties obtained with the PBE functional to the experimental ones for $TMS_2ZrCl_6$ and to avoid computational complexity and convergence issues one might encounter with hybrid functionals, all structures in this work were optimized using PBE approximation. For the electronic properties (band structure and DOS), due to the systematic and well-documented inaccuracy of the GGA level of theory, we employed the modified Becke–Johnson approximation (mBJ) [29,30] and screened hybrid functionals like Heyd–Scuseria–Ernzerhof HSE06 [31] and HSEsol [32]. We used the value of 400 eV for the maximum energy cutoff and a $2 \times 2 \times 2$ reciprocal space sampling. Moreover, our results concerning both the optimal structures and the bandgaps are highly converged with respect to reciprocal space sampling and energy cutoff. As we found, after changing the cutoff from 400 to 600 eV or the k-sampling from $2 \times 2 \times 2$ to $4 \times 4 \times 4$, the lattice constant variation is of the order of 1% while the bandgap is essentially unaffected.

## 3. Results and Discussion

### *3.1. $TMS_2ZrX_6$ (X = Cl, Br, I)*

At first, the experimentally determined crystal structure of $TMS_2ZrCl_6$ (data in SI of Ref. [20] as initial model) was fully energetically optimized using the GGA-PBE. The calculated structural characteristics, i.e., crystal symmetry, lattice parameters, and atomic coordinates, are in good agreement with the experimental ones [20]. For instance, the structural optimization resulted in a small reduction in the cell dimension by 0.028 Å compared to the experimental value. As expected, the calculated bandgap energy ($E_{gap}$) with GGA-PBE is not in agreement with the experimental one. Specifically, with GGA-PBE, we found a bandgap value of 3.88 eV for the experimental crystal structure and 3.92 eV for the optimized structure (see Figure 1). These bandgaps were found to be direct, and they are significantly smaller than the experimental value of 5.1 eV [20]. Note that the small increase in the bandgap energy is consistent with the fact that the optimization of the structure does not significantly affect the structural properties of the material.

As already mentioned, we calculated the electronic properties using mBJ, HSE06, and HSEsol approximations and adopting the structure that was optimized by the GGA-PBE functional. Our results are shown in Figure 2 and Table 1. As we see, these approximations significantly improve the values of $E_{gap}$. These values obtained by mBJ and HSE06 are 5.23 and 5.22 eV, respectively, approaching the experimental value of 5.1 eV. Note that attempts to optimize the structure via the mBJ, HSEsol, and HSE06 functionals either failed to

converge or were particularly time-consuming. Thus, we keep our single-point calculations using the GGA-PBE-optimized structure, which was very similar to the experimental one.

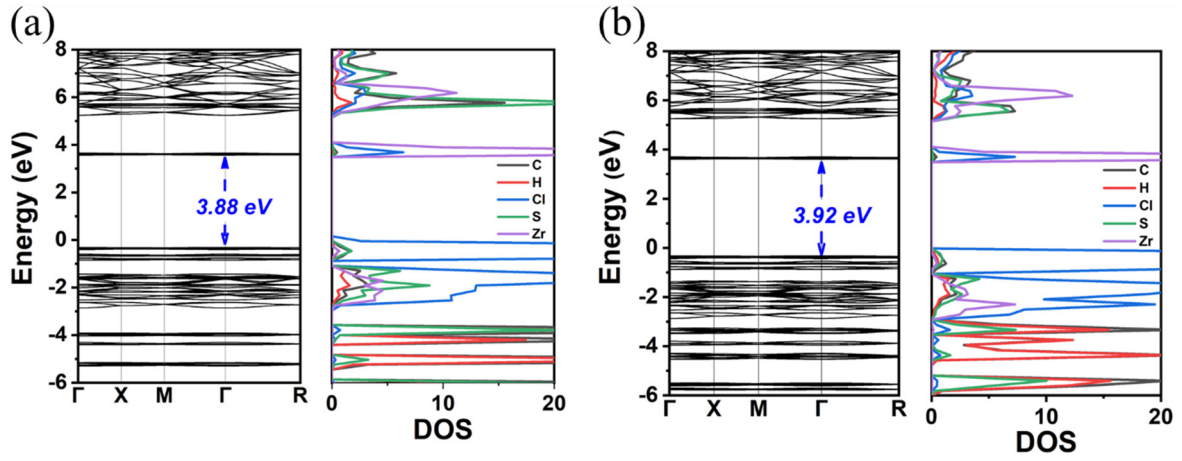


**Figure 1.** Calculated band structure and DOS of the (**a**) experimental crystal structure $TMS_2ZrCl_6$ and (**b**) energetically optimized crystal structure $TMS_2ZrCl_6$.

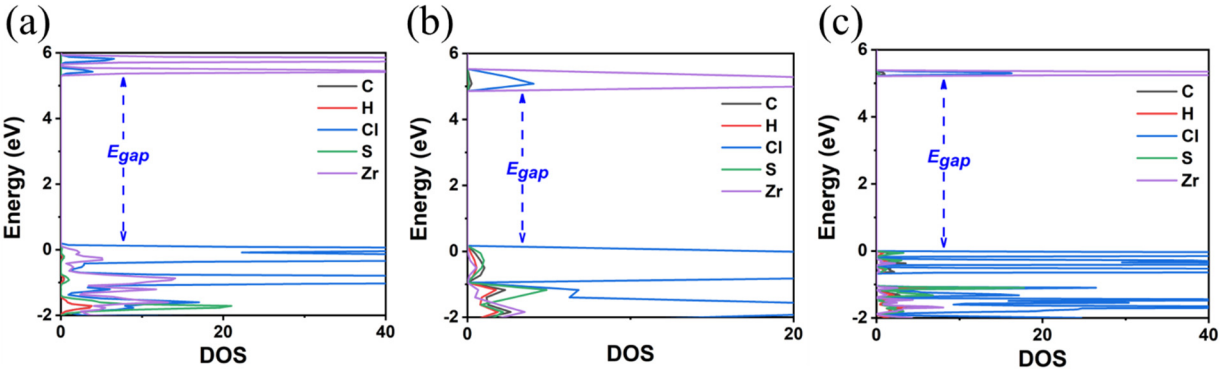


**Figure 2.** Calculated DOS of $TMS_2ZrCl_6$ using three different functionals: (**a**) Meta-GGA functional mBJ, (**b**) screened hybrid functional HSEsol, and (**c**) screened hybrid functional HSE06.

**Table 1.** Calculated values for bandgap energy in eV for $TMS_2ZrCl_6$ using various functionals.

| Functional | $E_{gap}$ |
|---|---|
| GGA-PBE | 3.92 |
| MBJ | 5.23 |
| HSEsol | 4.69 |
| HSE06 | 5.22 |
| Experimental [a] | 5.1 |

[a] Reference [20].

Furthermore, we studied the effect of X-site anion replacement on the electronic and structural properties of the $TMS_2ZrX_6$. The three different crystal structures of $TMS_2ZrCl_6$, $TMS_2ZrBr_6$, and $TMS_2ZrI_6$ are plotted in Figure 3. The corresponding lattice constants were calculated at 12.65 Å, 12.86 Å, and 13.49 Å, showing an increase of about 0.2 Å, due to the replacement of the Cl with the Br, and an additional increase of 0.6 Å, due to the replacement with the I anion. In all three compounds, the $[ZrX_6]^{2-}$ anions deviate only slightly from regular octahedral symmetry, with equatorial X–Zr–X angles at ca. 89.65° and 90.35°. The TMS cations retain their C3 rotational axis and adopt certain orientations in the unit cell (through this C3 axis and the electron lone pair of the S atom) with regard to the

[111] direction. The octahedra tilt significantly, namely by ca. 30°, considering the Zr–X–Zr angle for two octahedra along the [100] direction compared to the $K_2PtCl_6$ archetype. This tilt is stereochemically induced by the large TMS cation, without altering, though, the coordination environment of the Zr cations [33,34].

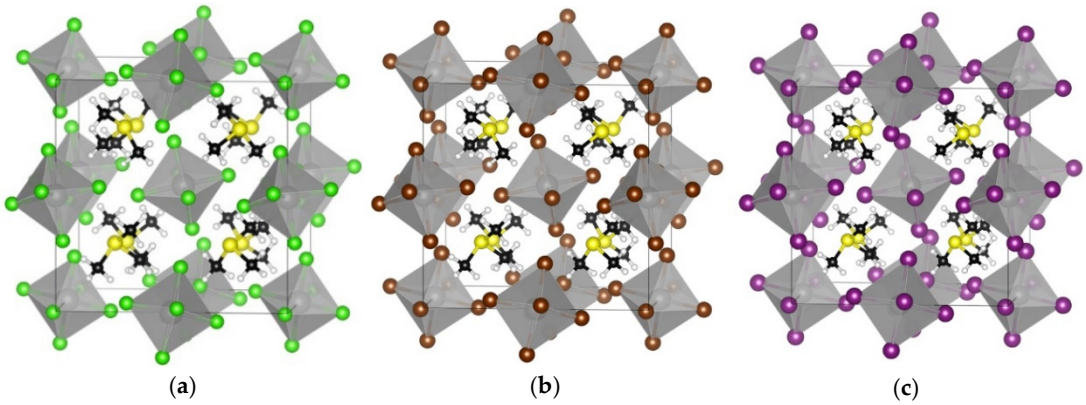


**Figure 3.** The optimized cubic crystal structures are shown for (**a**) $TMS_2ZrCl_6$, (**b**) $TMS_2ZrBr_6$, and (**c**) $TMS_2ZrI_6$. The images were created using VESTA software, version 3.90.1a [35]. Color assignment: yellow for S, black for carbon, white for hydrogen, grey for Zr, green for Cl, brown for Br, and violet for I.

Finally, the replacement of the X-site anion from Cl to Br and finally to I results in a decrease in the $E_{gap}$. Specifically, it was found that the reduction is Cl to Br 0.8(1.2) eV and Br to I 0.9(1.1) eV using the GGA-PBE(HSE06) functionals; see Figures 4 and 5 and Table 2. Given that for $TMS_2ZrCl_6$, the HSE06 $E_{gap}$ was calculated at 5.22 eV, in excellent agreement with the experimental gap of 5.1 eV, this functional is our best choice for the calculation of the bandgap energies, and we conclude that the $E_{gap}$ value of the $TMS_2ZrBr_6$ and $TMS_2ZrI_6$ are 4.05 eV and 2.97 eV, respectively; see Table 2. For comparison, the isostructural Sn compounds $TMS_2SnX_6$ exhibit experimental bandgaps of 4.1, 2.9, and 1.4 eV for X = Cl, Br, and I, respectively, and theoretical bandgaps of ca. 3.0, 2.0, and 0.9 eV for X = Cl, Br, and I, respectively, [36]. This effect is attributed mainly to more diffuse Sn orbitals compared to the Zr orbitals.

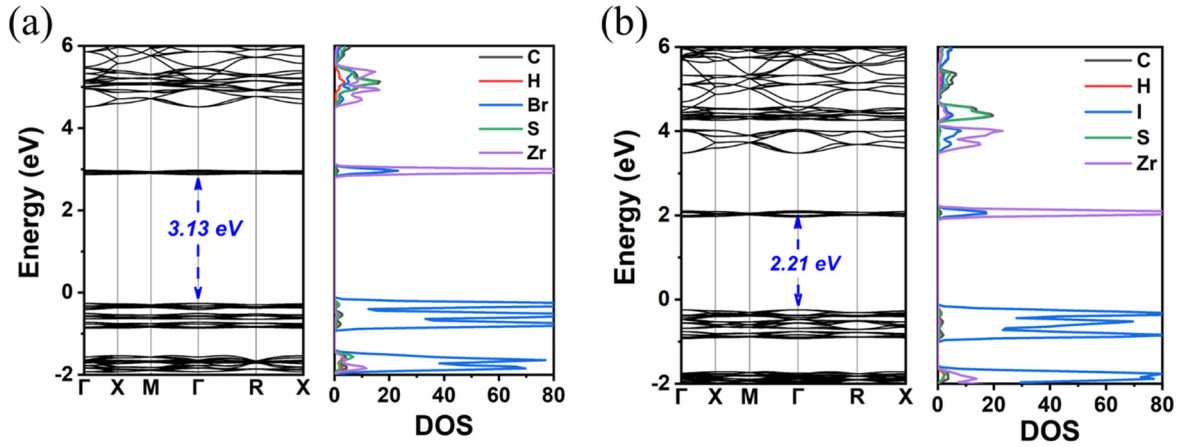


**Figure 4.** The calculated GGA-PBE band structure and DOS of (**a**) $TMS_2ZrBr_6$ and (**b**) $TMS_2ZrI_6$.

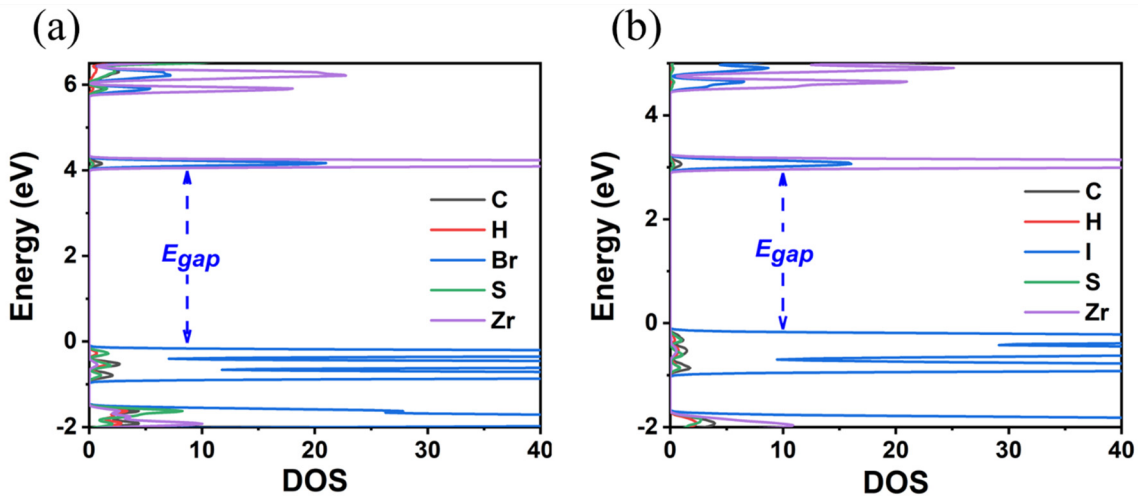


**Figure 5.** The calculated HSE06 DOS of (**a**) $TMS_2ZrBr_6$ and (**b**) $TMS_2ZrI_6$.

**Table 2.** Calculated bandgap energy, $E_{gap}$ (eV), lattice constants of the unit cell (Å), the shortest distance between halogen–halogen in the same octahedra, d* (Å), and in nearby octahedra, d** (Å) of $TMS_2ZrX_6$.

| Compound | $E_{gap}$ (GGA-PBE) | $E_{gap}$ (HSE06) | $E_{gap}$ Expt | Crystal System | Lattice Constants | d* | d** |
|---|---|---|---|---|---|---|---|
| $TMS_2ZrCl_6$ | 3.92 | 5.22 | 5.1 [a] | cubic | 12.65 | 3.51 | 4.90 |
| $TMS_2ZrBr_6$ | 3.13 | 4.05 | - | cubic | 12.86 | 3.73 | 4.78 |
| $TMS_2ZrI_6$ | 2.21 | 2.97 | - | cubic | 13.49 | 4.06 | 4.87 |

[a] Reference [20].

To sum up, we conclude that the increase in the atomic radius of the halogens (Cl < Br < I) results in an increase in the size of the unit cell by about 0.2–0.5 Å in each case. The halogen–halogen distance in the same octahedra increases when the atomic weight of the halogen increases. The decrease in the halogen electronegativity (Cl < Br < I) results in a decrease in the bandgap energy by about 1 eV in each case. Our best bandgap energies are obtained via the HSE06 functional, while the GGA-PBE significantly underestimated the $E_{gap}$ values.

### *3.2. $MA_2ZrX_6$ (X = Cl, Br, I)*

Additionally, we studied how the A-site cation replacement affects the structural and optoelectronic properties of $A_2ZrX_6$. In particular, the crystal structures of $MA_2ZrX_6$ were studied with three different halogens in the X-site anion, i.e., X = Cl, Br, and I. The obtained optimized crystal structures are all triclinic, see Figure 6 and Table 3, contrary to those of $TMS_2ZrX_6$, which are all cubic, as we have seen (Figure 3 and Table 2). This is attributed to the low symmetry of the MA cation and to the fact that as the structural refinement results in a certain orientation in order to form H bonds with the halogen atoms of the inorganic framework, the unit cell drops to triclinic symmetry. It is of note that the actual crystal structures of most perovskite compounds that contain MA and FA cations exhibit crystallographic disorder at room temperature due to the rotation of the cations [37]. The values of the lattice constants of the $MA_2ZrX_6$, see Table 3, increase with the replacement of the Cl with Br and finally with the I anion; similarly to the case of $TMS_2ZrX_6$, the lattice constants present an increase of about 0.4 Å, due to the replacement of Cl with Br, and an additional increase of 0.7 Å, due to the replacement of Br with I. The inorganic octahedra almost retain their regular shape, except for very small deviations in terms of both the

angles and bond lengths. A minor tilt of the octahedra of less than 1° is observed by using the same Zr–X–Zr notation as described above for $TMS_2ZrX_6$.

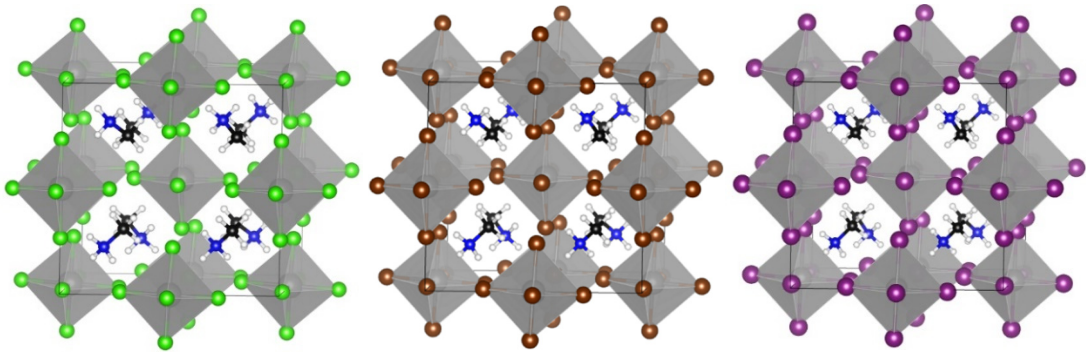

(**a**) (**b**) (**c**)

**Figure 6.** The optimized crystal structures of (**a**) $MA_2ZrCl_6$, (**b**) $MA_2ZrBr_6$, and (**c**) $MA_2ZrI_6$. The images were created using VESTA software, version 3.90.1a. Color assignment: blue for N, black for carbon, white for hydrogen, grey for Zr, green for Cl, brown for Br, and violet for I.

**Table 3.** Calculated bandgap energy, $E_{gap}$ (eV), lattice constants of the unit cell (Å), the shortest distance between halogen–halogen in the same octahedra, d* (Å), and in nearby octahedra, d** (Å) of $MA_2ZrX_6$.

| Compound | $E_{gap}$ (GGA-PBE) | $E_{gap}$ (HSE06) | Crystal System | Lattice Constants | | | d* | d** |
|---|---|---|---|---|---|---|---|---|
| | | | | a | b | c | | |
| $MA_2ZrCl_6$ | 2.88 | 4.06 | triclinic | 11.26 | 10.84 | 11.18 | 3.40 | 4.13 |
| $MA_2ZrBr_6$ | 2.11 | 3.14 | triclinic | 11.64 | 11.23 | 11.59 | 3.63 | 4.21 |
| $MA_2ZrI_6$ | 1.21 | 2.11 | triclinic | 12.30 | 11.92 | 12.28 | 3.98 | 4.39 |

Regarding the $E_{gap}$ values, as in the case of $TMS_2ZrX_6$, the replacement of the X-site anion from Cl to Br and finally to I results in a decrease in the $E_{gap}$ by about 1 eV; see Figures 7 and 8. The HSE06 functional is our best choice for calculating bandgap energies, and our predictions are 4.06 eV for $MA_2ZrCl_6$, 3.14 eV for $MA_2ZrBr_6$, and 2.11 eV for $MA_2ZrI_6$. Again, the GGA-PBE underestimates the bandgap energies by about 1 eV compared to HSE06, cf. Figures 7 and 8. Again, all bandgaps are direct.

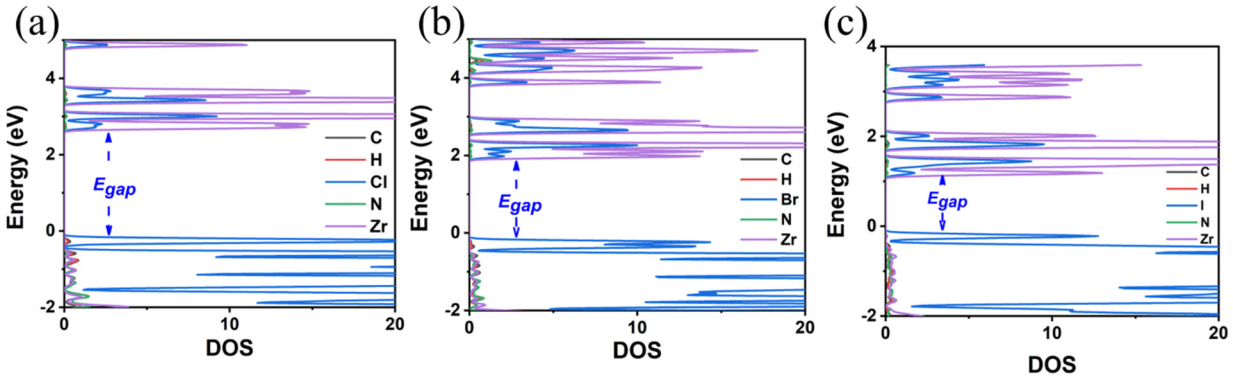


**Figure 7.** The calculated DOS of (**a**) $MA_2ZrCl_6$, (**b**) $MA_2ZrBr_6$, and (**c**) $MA_2ZrI_6$ using the GGA-PBE functional.

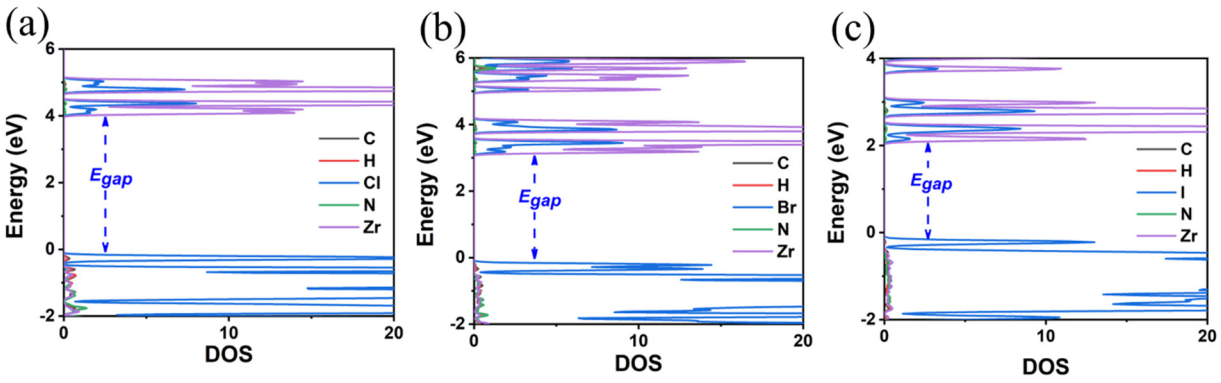


**Figure 8.** The calculated DOS of (**a**) $MA_2ZrCl_6$, (**b**) $MA_2ZrBr_6$, and (**c**) $MA_2ZrI_6$ using the HSE06 functional.

Comparing the $MA_2ZrX_6$ and the $TMS_2ZrX_6$ systems, it was found that the $MA_2ZrX_6$ presents significantly smaller bandgap energies by about 1 eV than the corresponding $TMS_2ZrX_6$ systems. This can be partly explained by the presence of a nitrogen atom in the MA, which is more electronegative than the sulfur atom found in the TMS, but also by the fact that the MA alters the crystal structure. Its smaller size compared to the TMS plays an important role in this structural alteration. Additionally, in both $MA_2ZrX_6$ and $TMS_2ZrX_6$, the primary contribution to VBM states comes from the halogen p-orbitals, while that of the CBM comes from the Zr d-orbitals. Although the contribution of the MA orbitals to the valence and conduction bands are small, the TMS to MA substitution substantially affects the structural features of the systems and, hence, indirectly influences the electronic properties, as indicated by the significant decrease in the bandgap energy.

### *3.3. $FA_2ZrX_6$ (X = Cl, Br, I)*

Finally, the crystal structures of $A_2ZrX_6$ were calculated, revealing the formamidinium cation in the A-site and X = Cl, Br, and I (Figure 9). The calculated optimal structures are all triclinic, as in the case of the MA, which is also due to the lower symmetry of the FA compared to the TMS. The lattice parameters and structural characteristics are given in Table 4. A tilt of ca. 5° from the ideal angle of 180° is observed in the octahedra. The FA groups are oriented diagonally between the adjacent inorganic layers, and the C atoms sit almost in the center of the cuboctahedral voids, which is the most symmetric and apparently thermodynamically favorable position.

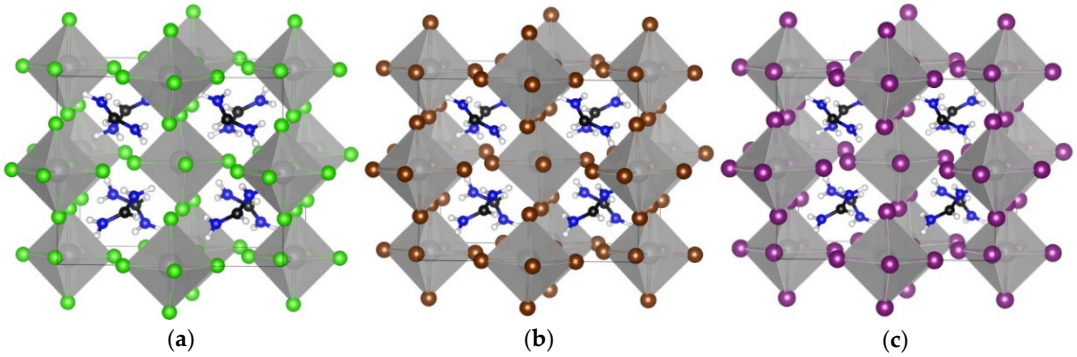


**Figure 9.** The optimized crystal structures are shown for (**a**) $FA_2ZrCl_6$, (**b**) $FA_2ZrBr_6$, and (**c**) $FA_2ZrI_6$. The images were created using VESTA software, version 3.90.1a. Color assignment: blue for N, black for carbon, white for hydrogen, grey for Zr, green for Cl, brown for Br and violet for I.

**Table 4.** Calculated bandgap energy, $E_{gap}$ (eV), lattice constants of the unit cell (Å), the shortest distance between halogen–halogen in the same octahedra, d* (Å), and in nearby octahedra, d** (Å) of $FA_2ZrX_6$.

| Compound | $E_{gap}$ (GGA-PBE) | $E_{gap}$ (HSE06) | Crystal System | Lattice Constants | | | d* | d** |
|---|---|---|---|---|---|---|---|---|
| | | | | a | b | c | | |
| $FA_2ZrCl_6$ | 3.70 | 4.81 | triclinic | 11.94 | 9.94 | 11.49 | 3.47 | 4.18 |
| $FA_2ZrBr_6$ | 2.87 | 3.89 | triclinic | 12.40 | 10.23 | 11.98 | 3.70 | 4.12 |
| $FA_2ZrI_6$ | 1.86 | 2.54 | triclinic | 13.04 | 10.80 | 12.69 | 4.02 | 4.37 |

In the final A-site cation substitution, both the electronic and structural properties are affected. The formamidinium cation, containing two electronegative nitrogen atoms, influences the bandgap energy. The $E_{gap}$ values are decreased compared to the TMS as the size of the halogen is increased, but are larger than those for the MA, as seen in Figures 10 and 11 and Table 4. DOS calculations using the HSE06 functional (see Figure 11) show that, for the FA, there is a significant contribution from N p-orbitals to the states close to VMB. This contribution is more pronounced for the Cl anion and decreases for Br and even more so for I. The HSE06 functional predicts bandgap energies of 4.81 eV ($FA_2ZrCl_6$), 3.89 eV ($FA_2ZrBr_6$), and 2.54 eV ($FA_2ZrI_6$).

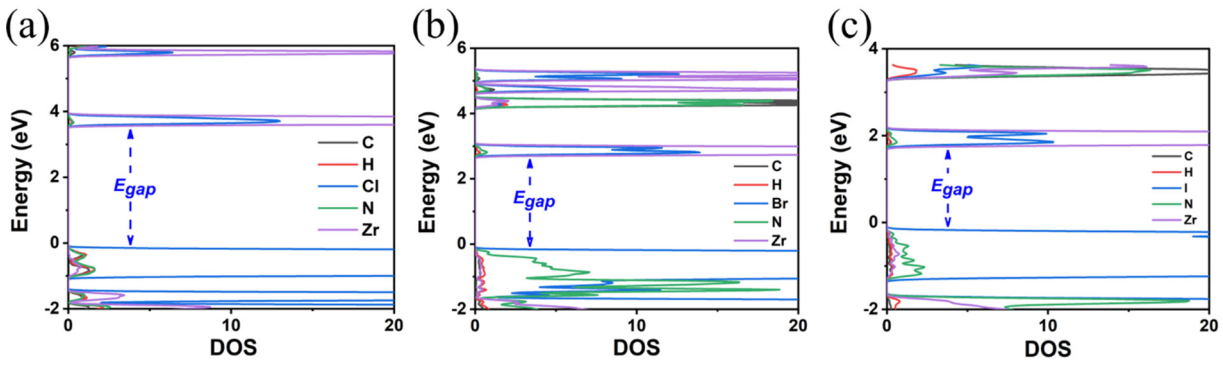


**Figure 10.** The calculated DOS of (**a**) $FA_2ZrCl_6$, (**b**) $FA_2ZrBr_6$, and (**c**) $FA_2ZrI_6$ using the GA-PBE functional.

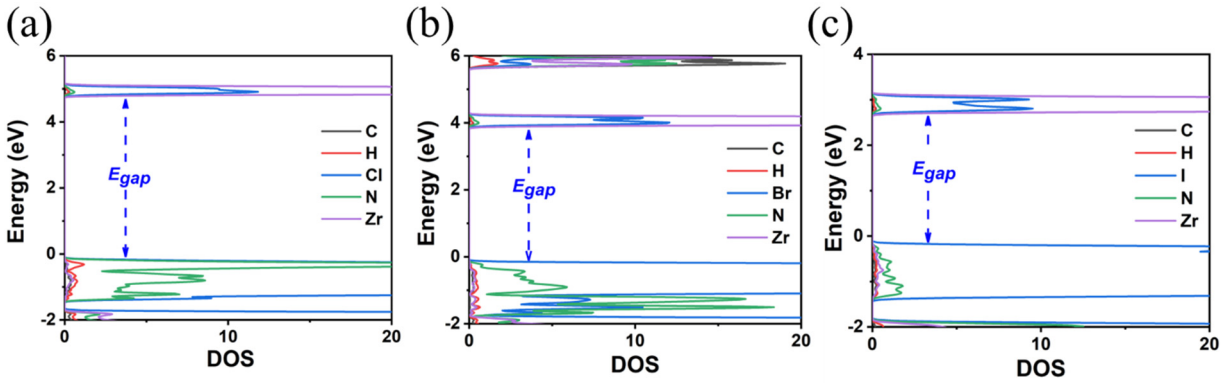


**Figure 11.** The calculated DOS of (**a**) $FA_2ZrCl_6$, (**b**) $FA_2ZrBr_6$, and (**c**) $FA_2ZrI_6$ using the HSE06 functional.

## 4. Trends

Two key findings emerge from this study. The first one concerns the effect of A-site cation substitution, and the second one concerns the effect of halogen substitution on the structural and electronic properties of the compounds.

*A-site cation substitution*: Regarding the structural characteristics, the $A_2ZrX_6$ structure type exhibits high stereochemical flexibility in order to accommodate different size cations, namely, in order of increasing sizes, Cs < MA < FA < TMS. Apart from the unit cell expansion and the change from the cubic to triclinic unit cell when incorporating cations with no symmetry (e.g., MA and FA), the octahedra tilt in order to accommodate large cations, such as the TMS. An alternative approach with regard to the volume of the organic cations, that takes into account the dynamic disorder within the crystal structure, is introduced by the term 'effective ionic radius' [38]. Based on this, the MA has an effective ionic radius of 2.17 Å and an FA of 2.53 Å. This difference also explains the larger unit cell volume found for the $FA_2ZrX_6$ series compared to the $MA_2ZrX_6$ series.

Changing the type and the effective ionic radius of the A-site cation substantially affects the bandgap energy, as seen in Figure 12. Note that both GGA-PBE and HSE06 present the same trends, although GGA-PBE significantly underestimates the gaps. In the case of the $TMS^+$, which is the biggest A-site cation and includes a sulfur atom, the bandgap is the largest. In the cases of the MA and FA, with one or two nitrogen atoms (more electronegative atoms), the bandgap decreases. The bandgaps for the MA are the smallest, indicating that $E_{gap}$ correlates also with the size of the A-site cation, decreasing as the size decreases.

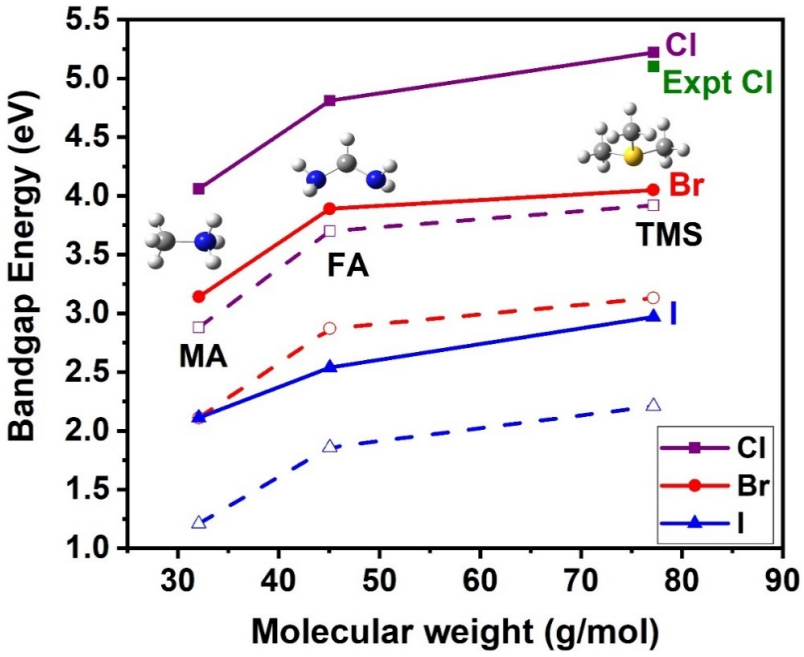


**Figure 12.** Bandgap energy as a function of the molecular weight of the A-site cation (g/mol) for the $A_2ZrX_6$ crystal, calculated using the HSE06 (solid lines) and GGA-PBE (dash lines) functionals. Available experimental value is also included [20]. Color assignment: blue for N, grey for carbon, white for hydrogen, yellow for S.

*X-site anion substitution:* The substitution of the X-site anion affects the electronic properties of the crystal structures. As the electronegativity of the X-site halogen is decreased, i.e., Cl > Br > I, the bandgap also decreases; see Figure 13. Both GGA-PBE and HSE06 present similar orbital type contributions for the VBM and CBM states. Our best results are obtained with the HSE06, which, in the case of the $TMS_2ZrX_6$ crystal, where experimental $E_{gap}$ is available, the HSE06 $E_{gap}$ is in excellent agreement with the experimental gap.

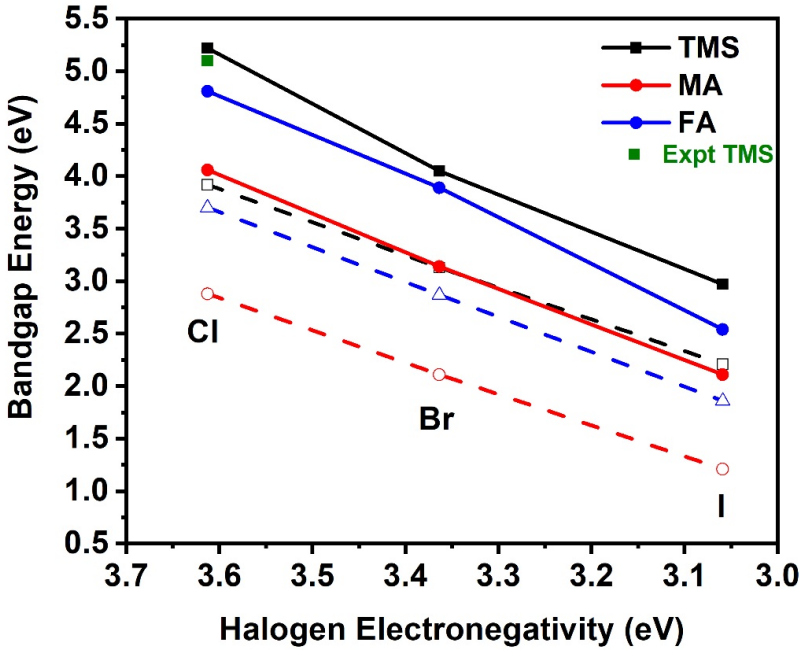


**Figure 13.** Bandgap energy as a function of halogen electronegativity of the $A_2ZrX_6$, calculated using the HSE06 (solid lines) and GGA-PBE (dash lines) functionals. Available experimental value is also included [20].

All the studied structures exhibit a wide range of bandgap energy that ranges from 5.22 eV to 2.11 eV. These perovskites are wide-bandgap semiconductors and, depending on their bandgap energy, are suitable for many applications in optoelectronics.

## 5. Conclusions

In the present paper, nine perovskites with the chemical formula $A_2ZrX_6$ have been studied, where the A-site cations are the methylammonium cation ($MA^+$), formamidinium cation ($FA^+$), and trimethylsulfonium cation ($TMS^+$) and the X-site anions are halogen, X = Cl, Br, and I. The crystal structures were studied using periodic DFT calculations with GGA-PBE, MBJ, HSEsol, and HSE06 functionals, employing the projected augmented wave (PAW) pseudopotential method. Our aim was to study a series of materials to determine the influence of the A-site cation or the X-site anion substitution on the bandgap energy and identify materials suitable for specific applications.

Our best bandgap energies were obtained with the HSE06 functional, which is in excellent agreement with the experiment concerning the bandgap energy of the $TMS_2ZrCl_6$ structure, while the GGA-PBE significantly underestimated the $E_{gap}$ by about 1 eV. Our predicted bandgap energies of the studied systems are 5.22 eV ($TMS_2ZrCl_6$; expt: 5.1 eV [20]), 4.05 eV ($TMS_2ZrBr_6$), 2.97 eV ($TMS_2ZrI_6$), 4.06 eV ($MA_2ZrCl_6$), 3.14 eV ($MA_2ZrBr_6$), 2.11 eV ($MA_2ZrI_6$), 4.81 eV ($FA_2ZrCl_6$), 3.89 eV ($FA_2ZrBr_6$), and 2.54 eV ($FA_2ZrI_6$). For comparison, the experimentally and theoretically studied $Cs_2ZrX_6$ compounds show bandgap values in the range of ca. 5 eV for $Cs_2ZrCl_6$ [17], ca. 3.8 eV for $Cs_2ZrBr_6$ [17], and ca. 3–3.7 eV for $Cs_2ZrBr_6$ [12].

Regarding the effect of halogen substitution on the structural and electronic properties of the considered systems, it was found that: The decrease in the halogen electronegativity (Cl < Br < I) or the increase in the halogen size results in an expansion of the unit cell and a decrease in the bandgap energy by about 1 eV in each case. Our result is consistent with the known trend of bandgap lowering in perovskites with the halogen substitution of the order (Cl → Br → I). However, the predicted energy gap values are still important information toward specific applications of these systems.

Concerning the A-site cation substitution, the increased electronegativity of the N-atom compared to the S-atom and the decrease in size for substitutions of the order (TMS → FA → MA) result in a unit cell contraction and a reduction in the bandgap. The bandgap energies are affected indirectly by the A-site substitution through the substantial modification of the structural features. The FA- and MA-based systems exhibit triclinic lattices, in contrast to the cubic lattices of TMS-based systems, due to symmetry lowering. Moreover, the larger size of the TMS compared to the FA and MA cations results in a significant tilt of the octahedra that deviates from the archetype 'defect' perovskite structure.

The systems under investigation are wide-bandgap semiconductors, and, depending on their bandgap energy, they are suitable as UV detectors and high temperature sensors, as thermal sensors, as photocatalysts, as thin-film transistors, in the design of deep UV light-emitting diodes, in high-power electronics, in the design of UV lasers, and in LEDs. Experimental investigations to synthesize these series of compounds are currently in progress.

**Author Contributions:** Conceptualization, C.K., N.N.L., A.K., I.D.P. and D.T.; Methodology, C.K., N.N.L., I.D.P. and D.T.; Validation, C.K., A.K., I.D.P. and D.T.; Formal analysis, C.K., N.N.L., A.K. and D.T.; Investigation, C.K., N.N.L. and D.T.; Resources, N.N.L., I.D.P. and D.T.; Data curation, C.K., N.N.L., A.K. and D.T.; Writing—original draft, C.K., N.N.L., I.D.P. and D.T.; Writing—review & editing, C.K., N.N.L., A.K., I.D.P. and D.T.; Visualization, C.K., A.K. and D.T.; Supervision, N.N.L., I.D.P. and D.T.; Project administration, N.N.L., A.K. and D.T.; Funding acquisition, N.N.L., A.K. and I.D.P. All authors have read and agreed to the published version of the manuscript.

**Funding:** This work was carried out within the framework of the Action 'Flagship Research Projects in challenging interdisciplinary sectors with practical applications in Greek Industry', implemented through the National Recovery and Resilience Plan Greece 2.0 and funded by the European Union—NextGenerationEU (Acronym: 3GPV-4INDUSTRY, project code: TAEDR-0537347).

**Data Availability Statement:** The original contributions presented in this study are included in the article. Further inquiries can be directed to the corresponding authors.

**Conflicts of Interest:** The authors declare no conflict of interest.

## References

1. Mitzi, D.B. Synthesis, Structure, and Properties of Organic-Inorganic Perovskites and Related Materials. *Prog. Inorg. Chem.* **2007**, *48*, 1–121.
2. Mitzi, D.B. Introduction: Perovskites. *Chem. Rev.* **2019**, *119*, 3033–3035. [CrossRef]
3. Arya, S.; Mahajan, P.; Gupta, R.; Srivastava, R.; Tailor, N.K.; Satapathi, S.; Sumathi, R.R.; Datt, R.; Gupta, V. A comprehensive review on synthesis and applications of single crystal perovskite halides. *Prog. Solid State Chem.* **2020**, *60*, 100286. [CrossRef]
4. Sharif, R.; Khalid, A.; Ahmad, S.W.; Rehman, A.; Qutab, H.G.; Akhtar, H.H.; Mahmood, K.; Afzal, S.; Saleem, F. A comprehensive review of the current progress and material advances in perovskite solar cells. *Nanoscale Adv.* **2023**, *5*, 3803–3833. [CrossRef] [PubMed]
5. Cui, J.; Liu, Y.; Deng, Y.; Lin, C.; Fang, Z.; Xiang, C.; Bai, P.; Du, K.; Zuo, X.; Wen, K.; et al. Efficient Light-Emitting Diodes Based on Oriented Perovskite Nanoplatelets. *Sci. Adv.* **2021**, *7*, eabg8458. [CrossRef] [PubMed]
6. Wang, C.; Meng, W.; Luo, G.; Xu, G.; Peng, M.; Xu, B.; Nie, S.; Deng, Z. RGB tri-luminescence in organic–inorganic zirconium halide perovskites. *Chem. Sci.* **2024**, *15*, 2954. [CrossRef]
7. Stranks, S.D.; Snaith, H.J. Metal-Halide Perovskites for Photovoltaic and Light-Emitting Devices. *Nat. Nanotechnol.* **2015**, *10*, 391–402. [CrossRef]
8. Xing, G.; Mathews, N.; Sun, S.; Lim, S.S.; Lam, Y.M.; Gratzel, M.; Mhaisalkar, S.; Sum, T.C. Long-Range Balanced Electron- and Hole-Transport Lengths in Organic-Inorganic $CH_3NH_3PbI_3$. *Science* **2013**, *342*, 344–347. [CrossRef]
9. Waser, R.; Dittmann, R.; Staikov, G.; Szot, K. Redox-Based Resistive Switching Memories-Nanoionic Mechanisms, Prospects, and Challenges. *Adv. Mater.* **2009**, *21*, 2632–2663. [CrossRef] [PubMed]
10. Reyren, N.; Thiel, S.; Caviglia, A.; Kourkoutis, L.F.; Hammerl, G.; Richter, C.; Schneider, C.W.; Kopp, T.; Ruetschi, A.-S.; Jaccard, D.; et al. Superconducting Interfaces Between Insulating Oxides. *Science* **2007**, *317*, 1196–1199. [CrossRef] [PubMed]

11. Zhang, Z.; Liang, Y.; Huang, H.; Liu, X.; Li, Q.; Chen, L.; Xu, D. Stable and Highly Efficient Photocatalysis with Lead-Free Double-Perovskite of Cs2AgBiBr6. *Angew. Chem. Int. Ed.* **2019**, *58*, 7263–7267. [CrossRef] [PubMed]
12. Cucco, B.; Katan, C.; Even, J.; Kepenekian, M.; Volonakis, G. Fine Structure of Excitons in Vacancy-Ordered Halide Double Perovskites. *ACS Mater. Lett.* **2023**, *5*, 52–59. [CrossRef]
13. Kojima, A.; Teshima, K.; Shirai, Y.; Miyasaka, T. Organometal halide perovskites as visible-light spensitizer for photovoltaic cells. *J. Am. Chem. Soc.* **2009**, *131*, 6050–6051. [CrossRef]
14. Kim, H.S.; Lee, C.R.; Im, J.H.; Lee, K.B.; Moehl, T.; Machioro, A.; Moon, S.J.; Baker, R.H.; Yum, J.H.; Moser, J.E.; et al. Lead iodide perovskite sensitized all-solid-state submicron thin film mesoscopic solar cell with efficiency exceeding 9%. *Sci. Rep.* **2012**, *2*, 591. [CrossRef]
15. Jeon, N.J.; Noh, J.H.; Yang, W.S.; Kim, Y.C.; Ryu, S.; Seo, J.; Seok, S.I.I. Compositional engineering of perovskite materials for high-performance solar cells. *Nature* **2015**, *517*, 476–480. [CrossRef] [PubMed]
16. Kaltzoglou, A.; Stoumpos, C.C.; Kontos, A.G.; Manolis, G.K.; Papadopoulos, K.; Papadokostaki, K.G.; Psycharis, V.; Tang, C.C.; Jung, Y.-K.; Walsh, A.; et al. Trimethylsulfonium lead triiodide: An air-stable hybrid halide perovskite. *Inorg. Chem.* **2017**, *56*, 6302. [CrossRef]
17. Abfalterer, A.; Shamsi, J.; Kubicki, D.J.; Savory, C.N.; Xiao, J.; Divitini, G.; Li, W.; Macpherson, S.; Gałkowski, K.; MacManus-Driscoll, J.L. Colloidal Synthesis and Optical Properties of Perovskite-Inspired Cesium Zirconium Halide Nanocrystals. *ACS Mater. Lett.* **2020**, *2*, 1644–1652. [CrossRef]
18. Dai, G.; Ma, Z.; Qiu, Y.; Li, Z.; Fu, X.; Jiang, H.; Ma, Z. Excitation-Dependent Luminescence of 0D $((CH_3)_4N)_2ZrCl_6$ across the Full Visible Region. *J. Phys. Chem. Lett.* **2022**, *13*, 7553–7560. [CrossRef]
19. Lin, J.-W.; Lu, X.; Liu, Z.; Lin, Y.-P.; Yang, J.; Ge, Y.; Zhou, C.; Wang, X.; Li, J.-R.; Du, K.-Z.; et al. Optical Property Regulation through Host–Guest Interaction in a Zero-Dimensional Zr Chloride. *Chem. Mater.* **2024**, *36*, 4600–4606. [CrossRef]
20. Tagiara, N.S.; Psycharis, V.; Kaltzoglou, A. Synthesis, crystal structure and luminescence of $[(CH_3)_3S]_2ZrCl_6$. *J. Coord. Chem.* **2024**, *77*, 286–294. [CrossRef]
21. Patterson, H.H.; Nims, J.L.; Valencia, C.M. Sharp-Line Luminescence of the Hexabromorhenate (IV) Ion in Single Crystal of Cesium Hexabromozirconate (IV) at 20 °K. *J. of Molec. Spectr.* **1972**, *42*, 567–574. [CrossRef]
22. Sinram, D.; Brendel, C.; Krebs, B. Hexa-iodoanions of Titanium, Zirconium, Hafnium, Palladium and Platinum: Preparation, Properties and Crystal Structures of the Caesium Salts. *Inorg. Chim. Acta* **1982**, *64*, L131–L132. [CrossRef]
23. Schroder, D.K. *Semiconductor Material and Device Characterization*; John Wiley & Sons, Inc.: Hoboken, NJ, USA, 2006.
24. *Wide Bandgap Semiconductors: Fundamental Properties and Modern Photonic and Electronic Devices*; Takahashi, K., Yoshikawa, A., Sandhu, A., Eds.; Springer: Berlin/Heidelberg, Germany, 2007.
25. Kresse, G.; Furthmuller, J. Efficiency of ab-initio total energy calculations for metal and semiconductors using a plane-wave basis set. *Comput. Mater. Sci.* **1996**, *6*, 15–50. [CrossRef]
26. Kresse, G.; Furthmuller, J. Efficient iterative schemes for ab initio total-energy calculations using a plane-wave basis set. *Phys. Rev. B.* **1996**, *54*, 11169–11186. [CrossRef]
27. Blochl, P.E. Projector augmented-wave method. *Phys. Rev. B* **1994**, *50*, 17953–17979. [CrossRef]
28. Perdew, P.; Burke, K.; Ernzerhof, M. Generalized Gradient Approximation Made Simple. *Phys. Rev. Lett.* **1996**, *77*, 3865–3868. [CrossRef]
29. Becke, A.D.; Johnson, E.R. A simple effective potential for exchange. *J. Chem. Phys.* **2006**, *124*, 221101. [CrossRef]
30. Tran, F.; Blaha, P. Accurate band gaps of semiconductors and insulators with a semilocal exchange-correlation potential. *Phys. Rev. Lett.* **2009**, *102*, 226401. [CrossRef]
31. Krukau, A.V.; Vydrov, O.A.; Izmaylov, A.F.; Scuseria, G.E. Influence of the exchange screening parameter on the performance of screened hybrid functionals. *J. Chem. Phys.* **2006**, *125*, 224106. [CrossRef] [PubMed]
32. Schimka, L.; Harl, J.; Krese, G. Improved hybrid functional for solids: The HSEsol functional. *J. Chem. Phys.* **2011**, *134*, 024116. [CrossRef] [PubMed]
33. Glazer, A.M. The Classification of Tilted Octahedra in Perovskites. *Acta Cryst.* **1972**, *B28*, 3384. [CrossRef]
34. Maughan, A.E.; Ganose, A.M.; Almaker, M.A.; Scanlon, D.O.; Neilson, J.R. Tolerance Factor and Cooperative Tilting Effects in Vacancy-Ordered Double Perovskite Halides. *Chem. Mater.* **2018**, *30*, 3909–3919. [CrossRef]
35. Momma, K.; Izumi, F. VESTA 3 for three-dimensional visualization of crystal, volumetric and morphology data. *J. Appl. Crystallogr.* **2011**, *44*, 1272–1276. [CrossRef]
36. Elsenety, M.M.; Kaltzoglou, A.; Antoniadou, M.; Koutselas, I.; Kontos, A.G.; Falaras, P. Synthesis, characterization and use of highly stable trimethyl sulfonium tin(IV) halide defect perovskites in dye sensitized solar cells. *Polyhedron* **2018**, *150*, 83–91. [CrossRef]

37. Manser, J.S.; Christians, J.A.; Kama, P.V. Intriguing Optoelectronic Properties of Metal Halide Perovskites. *Chem. Rev.* **2016**, *116*, 12956–13008. [CrossRef]
38. Kieslich, G.; Sun, S.; Cheetham, A.K. Solid-state principles applied to organic–inorganic perovskites: New tricks for an old dog. *Chem. Sci.* **2014**, *5*, 4712–4715. [CrossRef]